Applied Surface Science 567 (2021) 150793

Contents lists available at ScienceDirect

Applied Surface Science

journal homepage: www.elsevier.com/locate/apsusc

Full length article

Strain-induced structural phase transition in GeN monolayer

M. Abboud, D.H. Ozbey, E. Durgun *

UNAM - National Nanotechnology Research Center and Institute of Materials Science and Nanotechnology, Bilkent University, Ankara 06800, Turkey

ARTICLE INFO

Keywords:
2D materials
Phase transition
Strain engineering
ab initio

ABSTRACT

The recent synthesis of SiP, SiAs, GeP, and GeAs monolayers has brought two-dimensional (2D) group IV–V systems into the limelight. To date, all the fabricated structures of this class belong to the C2/m space group which has a low structural symmetry, while the class could exist in more symmetric phases (i.e., $P\bar{3}m1$ and $P\bar{6}m2$). The realization of more symmetric phases can enhance the intrinsic properties of these materials and increase their potential field of usage. In this study, the possibility of a structural phase transition in GeN monolayer by application of mechanical strain is investigated. Based on *ab initio* simulations, we first confirm the stability of the GeN monolayer in all phases, then demonstrate how a large enough compressive strain (~12%) can transform C2/m into $P\bar{3}m1$ phase. The results are interpreted by analyzing the geometry, bond order, electron localization functions, and net atomic charges of the structures. Upon transition into the $P\bar{3}m1$ phase, tensile strength and in-plane stiffness double, while the compressive strength quadruples. On the other hand, the effect of the phase transition on the electronic properties is not substantial and similar band structure profiles with narrowed band gap are obtained. Our study provides insight on how to experimentally achieve the $P\bar{3}m1$ phase of the GeN monolayer, which is in principle applicable to other group IV–V monolayers under suitable conditions involving the optimization of pressure, temperature, and impurity concentration. These unique features of the GeN monolayer render them ideal candidates for a variety of high technological nanoscale applications.

1. Introduction

Recent experimental developments in high-pressure melt growth have facilitated the fabrication of layered silicon and germanium monopnictides [1]. Their layers are separated by weak van der Waals (vdW) interactions and can be mechanically exfoliated into monolayers [1–3]. In fact, their exfoliation energy is comparable to that of graphite [2]. This experimental milestone has redirected the focus of theoretical and experimental research to group IV–V monolayers, in alignment with the increasing interest in novel two-dimensional (2D) materials with unique properties [4–7]. For instance, 2D SiP, which is a direct band gap semiconductor, has been used to produce a highly sensitive polarized light detectors [3,8]. GeP and GeAs monolayers have been experimentally studied for their optical, electrical, thermoelectric, anisotropic, and thickness-dependent properties [9–14]. Very recently, GeP monolayers have been utilized in making lithium- and sodium-ion batteries [15,16], likewise GeAs monolayers have been used to make field-effect transistors (FETs) and infrared photodetectors [14,17–19]. Together with the experimental efforts on this 2D class, theoretical studies predict that monolayers of group IV–V have desirable photocatalytic characteristics and can be used in solar water splitting [20–28]. It has also been shown that efficient energy conversion can be achieved by utilizing group IV–V monolayers, making them a good candidate for photovoltaic and solar cell applications [2,29–31]. Their excellent optical absorption, particularly in the visible and ultraviolet light ranges, suggests that they can potentially be used in optoelectronic devices [2]. In addition to these, tunability of their intrinsic properties via doping [2,32–38] and strain [30,39] has also been investigated.

To date, all the fabricated structures of the group IV–V class belong to the C2/m space group [1,9,14], while they could also exist in more symmetric $P\bar{3}m1$ and $P\bar{6}m2$ phases [40,41]. The realization of the more symmetric phases could enhance the physical properties of these structures and enrich their potential fields of usage. However, no guidelines have been reported on how to synthesize monolayers in $P\bar{3}m1$ and $P\bar{6}m2$ phases, or on the possibility of structural phase transition from C2/m to the energetically more favorable phases. For instance, strain engineering, which is a widely used technique to tune the properties of 2D materials [39,42–44], could be considered as a way to induce such structural phase transitions [45–49]. So far, the studies on group IV–V monolayers involving mechanical straining have been restricted to the elastic limit, yet a wider investigation beyond this regime is worth considering.

* Corresponding author.
E-mail address: durgun@unam.bilkent.edu.tr (E. Durgun).

https://doi.org/10.1016/j.apsusc.2021.150793
Received 11 April 2021; Received in revised form 10 July 2021; Accepted 27 July 2021
Available online 31 July 2021

2D GeN, which is a prominent member of the group IV–V class, have been predicted to be stable in three phases [27,40] and is a suitable candidate to examine the possibility of structural phase transition. It has been proposed as a potentially desirable material in variety of applications including electronics, sensors, energy conversion, and photocatalysis [27]. Historically, fabrication trials of low dimensional germanium nitride structures have been undergoing since the 1960s [50,51]. As fabrication and characterization techniques developed, the demand for ultra-thin GeN structures has grown significantly, and several different compositions have been synthesized by the late 1990s [52]. The recent successful fabrication of other group IV–V monolayers paves the way for realizing a GeN monolayer in the C2/m phase using similar techniques [1].

In this work, using first-principle simulations, we demonstrate the feasibility of achieving a structural phase transition (from C2/m to P$\bar{3}$m1) in the GeN monolayer through the application of a uniaxial strain along the armchair direction. Firstly, we validate the stability of the three phases of the GeN monolayer, then investigate the structural modifications under compressive and tensile strain. Next, the reasons that lead to phase transition are determined by analyzing the geometric and chemical properties of the bonds. Finally, the mechanical and electronic properties of GeN monolayer in P$\bar{3}$m1 symmetry are examined and compared with those of the C2/m phase.

2. Method

In this work, the Vienna *Ab initio* Simulation Package (VASP) [53] was used to perform first-principles calculations based on density functional theory with project-augmented wave (PAW) potentials [54]. Perdew–Burke–Ernzerhof (PBE) functional within the generalized gradient approximation (GGA) [53–55] was utilized for the exchange–correlation potential. GGA-PBE calculations were supplemented with Heyd–Scuseria–Ernzerhof hybrid functional (HSE06) to correct the underestimated electronic band gaps [56,57]. The cutoff energy was set to 530 eV and a vacuum space of 20 Å was placed along the non-periodic axis to prevent the artificial interactions. For the structural optimization and atomic relaxation, the Brillouin zone (BZ) was sampled uniformly by a 12 × 2 × 1 k-point mesh based on the Monkhorst–Pack scheme [58]. The convergence criteria for the electronic and ionic relaxation were set to 10^{-5} eV and 10^{-4} eV, respectively, the accuracy of which were confirmed to be adequate. For the *ab initio* molecular dynamics (AIMD) simulations, supercells with dimensions of at least 16 Å × 16 Å were considered to remove the size constraint. The AIMD simulations were performed using microcanonical ensemble by scaling the atomic velocities at 300 K, 600 K, and 900 K during 15 ps total simulation time with a time step of 1 fs.

The cohesive energy per atom (E_c) was calculated as follows:

$$E_c = \frac{E(\mathrm{GeN}) - N_{\mathrm{Ge}} \times E(\mathrm{Ge}) - N_{\mathrm{N}} \times E(\mathrm{N})}{N_{\mathrm{Ge}} + N_{\mathrm{N}}} \quad (1)$$

where E(GeN) is the total energy of GeN monolayer, E(Ge) and E(N) are the energies of single germanium and nitrogen atoms, respectively; and N_{Ge} and N_{N} are the number of germanium and nitrogen atoms per supercell, respectively.

ANSYS Workbench [59] was used to perform finite element analysis (FEA) on the structure. The uniaxial strain was calculated with respect to the relaxed pristine configuration as $\epsilon = (b - b_0)/b_0$ where b and b_0 are the strained and pristine cell dimensions respectively, while the stress was calculated as $\sigma = \frac{1}{A_0}\frac{\partial E}{\partial \epsilon}$, where A_0 is the area of rectangular supercell. Tests along the zigzag and armchair directions were performed separately.

3. Results and discussion

We start with the optimization of a GeN monolayer in the C2/m phase, since the lattice of all the realized 2D group IV–V systems belongs to this space group. The structure of the C2/m-GeN is shown in Fig. 1(a) where the unit cell used in the calculations is defined by a black frame containing 12 Ge and 12 N atoms. The unit cell is identical to traditionally considered unit cells for group IV–V monolayers of the C2/m phase [1,2,25,27,39]. The optimized lattice constants are **a** = 3.10 Å and **b** = 18.82 Å, representing the zigzag and armchair directions, respectively. The obtained values are in agreement with the literature [27]. The lattice constants of GeN monolayer are expectedly shorter than those of GeP and GeAs, as N is smaller than P and As atoms. The C2/m unit cell has unequal lattice constants where the cell is highly elongated in the armchair direction (**b** ≈ 6**a**). While each N atom is coordinated to three Ge atoms, Ge atoms are coordinated to three N atoms and one Ge atom. Thus, four types of bonds can be identified in the C2/m phase; α(Ge-N), β(Ge-N), α(Ge-Ge), and β(Ge-Ge) bonds, which are calculated as 1.92 Å, 1.92 Å, 2.48 Å, and 2.46 Å, respectively. All the bonds are labeled on the side view of the GeN monolayer in Fig. 1(a). The cohesive energy (E_c) of C2/m-GeN is found to be 4.30 eV/atom, which is higher than that of GeP (3.84 eV/atom) and GeAs (3.62 eV/atom).

To confirm the stability of the structure, AIMD simulations are performed starting at 300 K, and the temperature is gradually increased to 900 K within 15 ps total simulation time. The fluctuation of the total energy (E_{fluct}) is computed as the change of total energy in percentage at each step with respect to the average energy of the system. Fig. 1(b) presents E_{fluct} during the AIMD simulations of C2/m-GeN as well as the snapshots of the structure at the end of each simulation. Since E_{fluct} does not exceed 1% and the distortions in the final structure are minimal, it can be concluded that the structures are dynamically stable. Additionally, the calculated phonon spectrum (see Fig. S1 in the Supplemental Material [60]) is free from any imaginary frequencies, which together with the AIMD simulations validate the stability of the C2/m-GeN monolayer [27].

Next, uniaxial strain is applied on a C2/m-GeN monolayer along zigzag and armchair directions to investigate possible structural phase transitions. No significant structural modifications are noticed when tensile and compressive strain are applied along zigzag direction (see Fig. S2 in the Supplemental Material [60]). While tensile strain along the armchair direction does not change the phase of the C2/m-GeN monolayer, a phase transition into P$\bar{3}$m1 is detected upon applying a uniaxial compressive strain of ~12%. Fig. 2 shows the evolution of total energy during the compression of C2/m-GeN that leads to a phase transition into P$\bar{3}$m1. As P$\bar{3}$m1 is of a lower energy configuration than C2/m, a sudden drop of energy is noticed at the point of the phase transition. The test continues beyond the phase transition point and the results beyond that strain level are analogous to compressing pristine P$\bar{3}$m1 structure. The obtained structure is confirmed to be identical to that of a pristine P$\bar{3}$m1-GeN monolayer with the same lattice constants. The C2/m phase overcomes an energy barrier of ~2.9 eV to transform into an energetically more favorable P$\bar{3}$m1 phase. It should be noted that, phase transition is not reversible, for instance C2/m phase is not obtained with tensile strain once started from the P$\bar{3}$m1 phase. The tests are repeated for the other possible phase (P$\bar{6}$m2), and no structural phase transition is noticed (see Fig. S2 in the Supplemental Material [60]). For the sake of comparison, strain is applied on three phases of GeP and GeAs monolayers up to failure and these tests do not lead to any structural modification (see Fig. S3 in the Supplemental Material [60]) as C2/m is the lowest energy configuration for these systems different from GeN. It should be noted that these tests are performed by using ground-state method (i.e., the effect of temperature is not included), and therefore the obtained results do not fully exclude the possibility of strain-induced phase transitions in other 2D group IV–V systems when external factors (e.g., temperature, pressure, defects, vacancies, or a substrate effect) are taken into account and controlled.

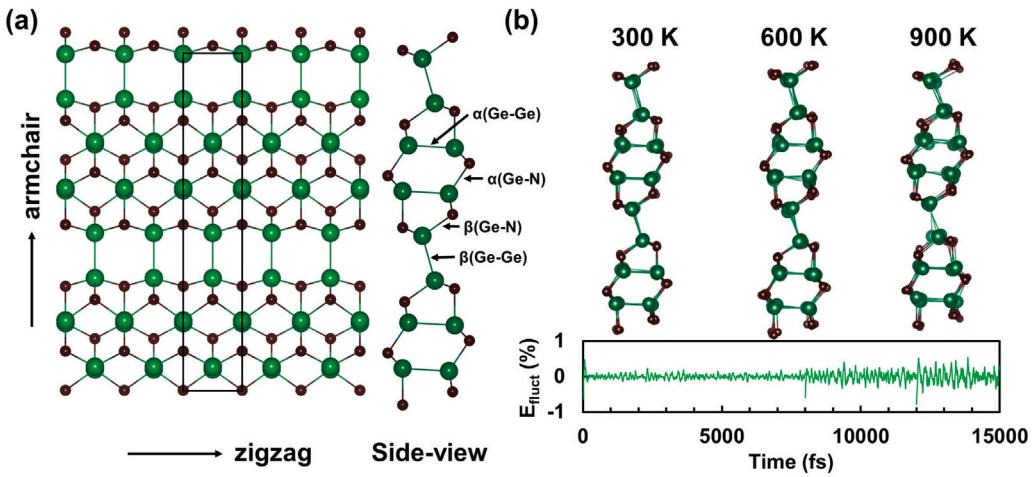

Fig. 1. (a) The top and side views of the C2/m-GeN structure. The unit cell is shown with a solid rectangle. (b) The fluctuation of total energy during the AIMD simulations and the snapshots of the structure at the end of each simulation. The green and purple spheres represent Ge and N atoms, respectively.

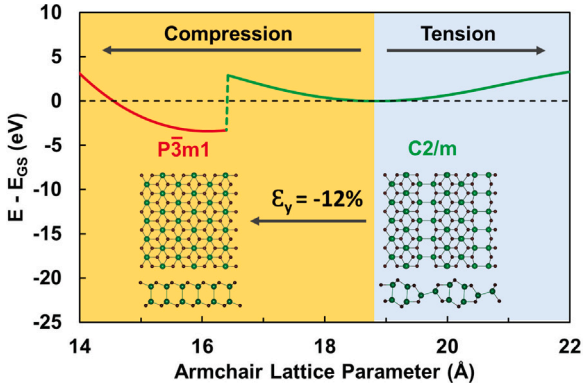

Fig. 2. Evolution of total energy as a function of armchair lattice parameter during the compression and tension of C2/m-GeN. The total energy of C2/m-GeN at equilibrium (E_{GS}) is taken as a reference.

As mentioned above, the strain-induced system is identical to the P$\bar{3}$m1 phase of GeN reported in the literature [40]. P$\bar{3}$m1-GeN is energetically more favorable than C2/m-GeN, which indicates the possibility of achieving P$\bar{3}$m1 phase directly, in addition to strain engineering.

The structure of P$\bar{3}$m1-GeN is presented in Fig. 3(a) where the supercell with rectangular lattice is defined with a black frame containing 12 Ge and 12 N atoms. The dimensions of the supercell are **a** = 3.10 Å and **b** = 16.10 Å. While both phases have the same **a**, **b** of P$\bar{3}$m1 is shorter than that of the C2/m phase. The configuration of P$\bar{3}$m1-GeN is more symmetrical than C2/m-GeN and has only two types of bonds; α(Ge-N) bonds which are 1.91 Å, and α(Ge-Ge) bonds which are 2.54 Å. It should be noted that E_c of P$\bar{3}$m1-GeN is found to be 4.44 eV/atom, which is higher than that of C2/m-GeN. Similar to the C2/m phase, AIMD simulations are performed to test the dynamical stability of the system. Only small distortions are noticed in the structure even at 900 K, and E_{fluct} fluctuates within a range of less than 1%, validating the stability of the GeN monolayer in the P$\bar{3}$m1 phase. Fig. 3(b) shows the fluctuation of total energy (E_{fluct}) with time and snapshots of structures at the end of each simulation. Phonon spectrum analysis further confirms the dynamical stability of P$\bar{3}$m1-GeN monolayer (see Fig. S1 in the Supplemental Material [60]). The structural stability at high temperatures also eliminates the limitations on applying strain at elevated temperatures.

Thereafter, the factors that lead to the phase transition are investigated. When the C2/m-GeN structure is examined at each step of the compression, it is noticed that the β(Ge-Ge) bonds are deforming the most. At the onset of the phase transition, the β(Ge-Ge) bonds shrink by ~5.5%, the α(Ge-Ge) bonds expand by ~2.4%, while Ge-N bonds remain almost intact. The fact that the character of Ge-N bonds are identical in both phases, makes the phase transition from C2/m to P$\bar{3}$m1 plausible. In both compression and tension cases, rupture happens only along the β(Ge-Ge) bonds. It is worth mentioning that even though the P$\bar{6}$m2 phase share bonding similarities with C2/m, it has a very different Ge-N bonding orientations rendering the transition from C2/m to P$\bar{6}$m2 infeasible.

The β(Ge-Ge) bonds in the C2/m phase are not only potential stress concentration sites, but are also intrinsically weaker than the rest of the bonds in the structure. Thus, the geometrical factors are also investigated using FEA [59,61], a tool that can be used to compute stresses and deformations in 2D materials such as graphene sheets [62,63]. The force distributions along the bonds on pristine C2/m and P$\bar{3}$m1 structures are estimated by fixing one end and applying a constant force on the opposite end. All the axial and shear forces acting on the bonds are obtained as percentages of an applied force along armchair direction. The axial and shear force distributions in both of the phases are given Fig. 4(a)–(b). As can be seen from Fig. 4, for the C2/m phase, the β(Ge-Ge) bonds receive 96% of the applied force as an axial force, while the rest of the bonds receive less than 70% of the force. This shows that there is a higher stress concentration at the β(Ge-Ge) bonds. On the contrary, the axial forces are more homogeneously distributed along the bonds in the P$\bar{3}$m1 phase. The α(Ge-Ge) bonds, which are perpendicular to the direction of the applied force, show a slightly negative axial force. Similar to the axial forces, the shear forces are distributed uniformly in P$\bar{3}$m1, while in the C2/m phase shear stresses are the highest at the Ge-N bonds in connection with the β(Ge-Ge) bonds in C2/m.

In addition to calculating the stress distributions, bond orders, which have a direct correlation with bond strengths are computed [64, 65] using the DDEC6 method [66]. Fig. 5(a) shows the local bond orders (LBO) of the bonds projected onto C2/m and P$\bar{3}$m1 structures. It is evident that in both phases the Ge-Ge bonds have a lower LBO than the Ge-N bonds. In the C2/m phase, β(Ge-N) bonds, which are connected to the β(Ge-Ge) bonds, have a lower LBO (~0.77) than the α(Ge-N) bonds (~0.90). The summation of all bond orders of an atom (SBO) helps to estimate the tendency of an atom in a specific position to relocate into a more favorable position. In other words, if large enough strain is applied, the atom that has a lower than average SBO is the first to be relocated within the structure. For both C2/m and P$\bar{3}$m1, SBO on each atom in the supercell is calculated by considering all neighboring atoms that have a considerable contribution (i.e., 50 neighboring atoms). For C2/m, the Ge atoms that are forming the

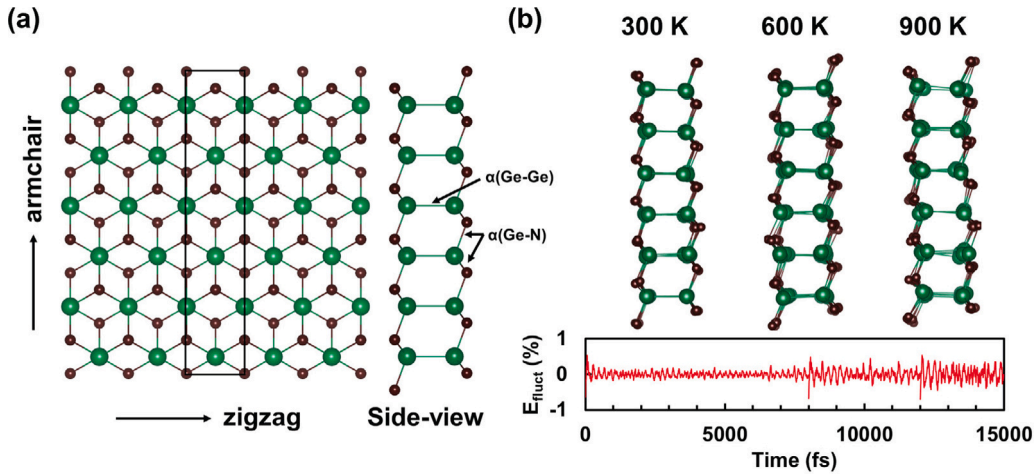

Fig. 3. (a) The top and side view of GeN monolayer in P$\bar{3}$m1 phase. The supercell is shown with solid rectangle. (b) The fluctuation of total energy during the AIMD simulations and the snapshots of the structure at the end of each simulation. The green and purple spheres represent Ge and N atoms, respectively.

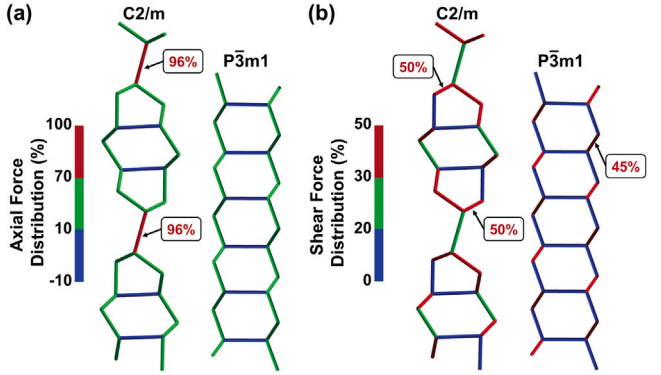

Fig. 4. Finite element analysis (FEA) of (a) axial and (b) shear force distributions on C2/m and P$\bar{3}$m1 phases.

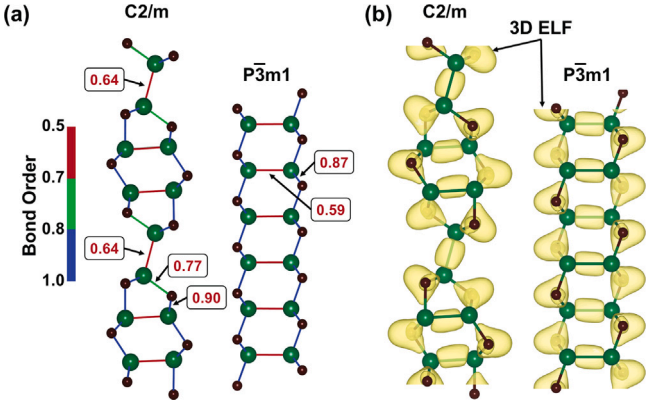

Fig. 5. (a) Local bond orders projected on the bonds of C2/m- and P$\bar{3}$m1-GeN, and (b) electron localization function (ELF) profiles. The green and purple spheres represent Ge and N atoms, respectively.

β(Ge-Ge) bonds have SBO of 3.65 each, while Ge atoms that form the α(Ge-Ge) bonds have SBO of 3.89 on average. This means that the β(Ge-Ge) bonds more prone to structural change than the α(Ge-Ge) bonds. In contrast, each N atom in C2/m has SBO of 2.68, which is homogeneous and there is no tendency of structural modification around a specific N atoms. In the case of the P$\bar{3}$m1 phase, each Ge and N atom has SBO of 3.87 and 2.78, respectively. This uniformity in the P$\bar{3}$m1 phase indicates that any stress applied would affect the structure homogeneously. Therefore, the phase transition occurs at the β(Ge-Ge) bonds which are not only stress concentration cites but also weaker than the rest of the bonds in C2/m-GeN.

While bond orders quantify the strength of the bonds, electron localization function (ELF) [67,68] gives an insight into the reasons that make Ge-Ge bonds intrinsically weaker than Ge-N ones. The electron localization between atoms indicates covalent bonding, while the localization around atoms indicates charge gain. Fig. 5(b) shows the ELF profiles of valence electrons (with isosurface higher than 0.75) on the side-views of C2/m- and P$\bar{3}$m1-GeN. In both phases, electron localization around N atoms and along the Ge-N bonds indicates that Ge-N bonds have covalent and ionic character, while the electron localization along the Ge-Ge bonds implies that these bonds are mainly covalent. Since N atoms possess a higher electron affinity and electronegativity than Ge atoms [69], charge donation from Ge to N atoms is anticipated. In terms of bond strength, it can be said that Ge-N bonds are strengthened by both covalent and ionic interactions, while the homonuclear Ge-Ge bonds are much weaker due to the lack of ionic contributions. Similar behavior is also observed in other group IV–V monolayers [39].

Having demonstrated and justified the phase transition in the GeN monolayer, we compare the physical properties of both phases starting from their mechanical response. Fig. 6(a) shows the stress–strain curves of C2/m and P$\bar{3}$m1 phases during both the compression and tension tests. The phase transition strain level of C2/m (12%) is marked by a dotted line. The fact that the curve is almost linear until the phase transition occurs, suggests that the transition happens before any significant plastic deformation. Furthermore, it is evident in Fig. 6(a) that the P$\bar{3}$m1 phase has superior strength in both compression and tension cases. While both phases fracture under the same amount of tensile strain (~19%), P$\bar{3}$m1 phase fails at 16.2% compressive strain, resisting a 3.3% more than the C2/m phase, demonstrating an improvement in ductility. The maximum tensile stress that the phase P$\bar{3}$m1 can withstand without failing (15.2 N/m) is more than twice that of C2/m (6.7 N/m), and the maximum compressive stress that the phase P$\bar{3}$m1 can resist before fracture (48.8 N/m) is more than four times that of C2/m (11.7 N/m). That is, significant enhancement in ultimate tensile/compressive strength can be achieved by the strain-induced phase transition. The slope of the curves also indicate that P$\bar{3}$m1-GeN is more elastic than C2/m-GeN. To accurately compute the elastic properties, a separate calculation is performed to obtain the elastic constants (C_{ij}). These constants can be used to obtain the angle-dependent in-plane stiffness (Y_{2D}) and the Poisson's ratio (ν) according to the following

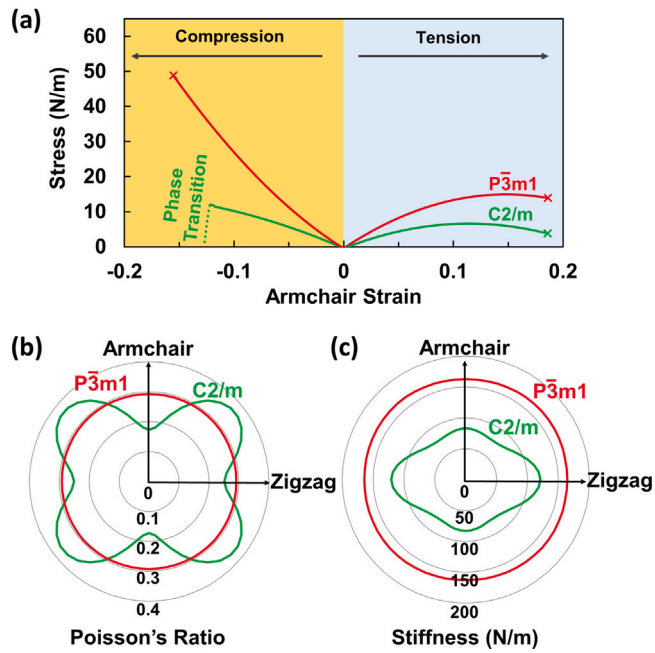

Fig. 6. (a) The stress–strain curves, (b) angle-dependent Poisson's ratio, and (c) angle-dependent in-plane stiffness of the C2/m- and P$\bar{3}$m1-GeN monolayer.

Table 1
Summary of the mechanical properties of the C2/m- and P$\bar{3}$m1-GeN in zigzag and armchair directions.

Property	Zigzag		Armchair	
	C2/m	P$\bar{3}$m1	C2/m	P$\bar{3}$m1
In-plane stiffness (N/m)	120.7	158.8	82.9	158.8
Tensile strength (N/m)	14.9	16.4	6.7	15.2
Comp. strength (N/m)	76.0	87.2	11.7	48.8
Poisson's ratio	0.25	0.29	0.18	0.29
Max. tens. strain	25.8	25.8	19.1	19.3
Max. comp. strain	19.4	22.6	12.9	16.2

formulas [70],

$$Y_{2D}(\theta) = \frac{A}{C_{11}\, s^4 + C_{22}\, c^4 + (B - 2\, C_{12})\, c^2\, s^2} \tag{2}$$

$$\upsilon(\theta) = -\frac{(C_{11} + C_{22} - B)\, c^2\, s^2 - C_{12}\,(c^4 + s^4)}{C_{11}\, s^4 + C_{22}\, c^4 + (B - 2\, C_{12})\, c^2\, s^2} \tag{3}$$

where $c = cos(\theta)$, $s = cos(\theta)$, $A = (C_{11}\, C_{22} - C_{12}^2)$, and $B = (\frac{C_{11}\, C_{22} - C_{12}^2}{C_{66}})$.

The obtained values of $Y_{2D}(\theta)$ and $\nu(\theta)$ are shown in Fig. 6(b)–(c). (The comparison of $Y_{2D}(\theta)$ and $\nu(\theta)$ for all phases is shown in Fig. S4 in the Supplemental Material [60]) While $Y_{2D}(\theta)$ and $\nu(\theta)$ are anisotropic for C2/m [39], they become isotropic for P$\bar{3}$m1 phase. Y_{2D} of P$\bar{3}$m1 is larger than that of C2/m and enhancement is more significant along armchair direction (i.e., in-plane stiffness is almost doubled after the phase transition). In a similar manner ν also increases for the P$\bar{3}$m1 phase along armchair direction. However, ν lies within the same range as of most well-known engineering materials such as metals, polymers, and ceramics [71]. In addition, as $\nu(\theta) < 0.33$, both phases are brittle in compliance with the Christensen rule [72]. The calculated mechanical properties are summarized in Table 1 and reveal that the mechanical response of P$\bar{3}$m1 phase is superior than the C2/m phase. The reasons for the enhancement in mechanical performance are the higher symmetry and isotropy obtained after the removal of the weak β(Ge-Ge) bonds which are stress concentration sites, have a low bond order, and lack of ionic contributions.

Finally, the effect of phase transition on the electronic properties of the GeN monolayer is investigated. The electronic band structures and the band gaps calculated at the level of GGA-PBE (E_g^{PBE}) and HSE (E_g^{HSE}) methods for both phases are shown in Fig. 7(a). The E_g^{PBE} (E_g^{HSE}) for C2/m and P$\bar{3}$m1 are 1.35 eV and 1.11 eV (2.36 eV and 2.19 eV), respectively. The obtained band gaps are in the visible-light spectrum and within the range of obtained band gaps for SiP, SiAs, GeP, and GeAs (E_g^{HSE} = 2.08–2.64 eV). Both phases of GeN are indirect band gap semiconductors, which is a common characteristic for most group IV–V monolayers [2,25,40]. Nonetheless, band convergence is obtained along $\Gamma - X$ for the valence band maximum of P$\bar{3}$m1-GeN and the system becomes almost direct, which can lead to enhanced thermoelectric performance [73]. The electronic band structures of the two phases are similar, however band separation is noticed in the P$\bar{3}$m1 phase at Γ-point for valence band maximum (VBM) and conduction band minimum (CBM), resulting in a narrowed band gap. The projected density of states (PDOS) shown in Fig. 7(a) indicate that VBM and CBM of both phases have similar character. The net atomic charge distributions are resemble in both phases as shown in Fig. 7(b). In both phases, the net atomic charge on N atoms is between −0.75 and −0.6, while it is between +0.6 and +0.75 for Ge atoms.

The similarities in the electronic band structure and PDOS can be explained by the fact that the two phases possess similar bond order, ELF, and atomic charge distributions. While difference in geometry and structure of C2/m and P$\bar{3}$m1 significantly improves mechanical properties, the alternation on the electronic structure is not substantial. For instance even though the band gap narrows following the structural phase transition from C2/m and P$\bar{3}$m1, it remains in the visible spectrum.

The applied strain is also expected to modify the band gaps of both phases within the elastic regime. Fig. 8 shows the variation of E_g^{PBE} of C2/m and P$\bar{3}$m1 phases under uniaxial strain in the armchair direction. The corresponding band structures are shown in Figs. S5–S8 in the Supplemental Material [60]. For the P$\bar{3}$m1 phase, the band gap widens as the system is compressed and narrows as the system is stretched. The P$\bar{3}$m1-GeN structure becomes a metal once the tensile strain exceeds 8%. The decrease after -6% strain is attributed to the plastic deformation of the structure. C2/m phase follows a similar trend under tension, however, the band gap decreases more slowly with tensile strain. On the other hand, the band gap narrows for compressive strain and converges to that of P$\bar{3}$m1-GeN as strain approaches the phase transition level.

4. Conclusion

In summary, we investigated the strain-induced structural phase transition in the GeN monolayer. Firstly, through *ab initio* molecular dynamics simulations, the stability of the GeN monolayer in its various phases is confirmed. Next, uniaxial compressive and tensile strain along possible orientations is applied and a structural phase transition is noticed upon compressing a C2/m-GeN monolayer 12% along the armchair direction. The obtained structure belongs to the previously predicted P$\bar{3}$m1 phase, and is a lower energy configuration. The reasons for this phase transition are: (1) the fact that both lattices only differ in the armchair direction but are identical in the zigzag direction, (2) the structural similarity between C2/m and P$\bar{3}$m1 phases, (3) nitrogen atoms are small and can relocate without breaking the strong Ge-N bonds, and (4) the existence of less stable β(Ge-Ge) bonds. Moreover, the factors that weaken the β(Ge-Ge) bonds are: (1) the geometrical disadvantage which causes a stress concentration along and around them, (2) the lower bond order, and (3) the lack of ionic contributions in the Ge-Ge bonds in general. Additionally, it is revealed that the more symmetric P$\bar{3}$m1 phase is mechanically superior to the C2/m phase. For instance, upon phase transition into P$\bar{3}$m1, tensile strength and in-plane stiffness double, while the compressive strength quadruples. This enhanced mechanical response is mainly due to the absence of β(Ge-Ge)

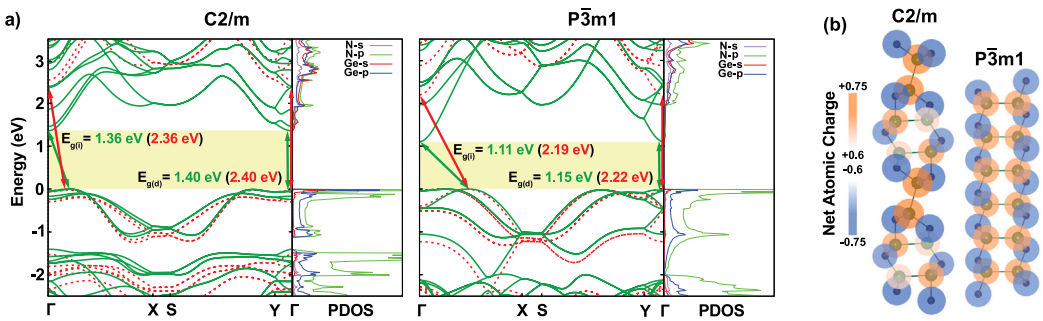

Fig. 7. (a) The electronic band structures, projected density of states (PDOS), and (b) net atomic charge distributions of C2/m- and P$\bar{3}$m1-GeN monolayer. The solid green and red dashed lines corresponds to PBE and HSE06 results, respectively. The direct ($E_{g(d)}$) and indirect ($E_{g(i)}$) band gaps are also shown.

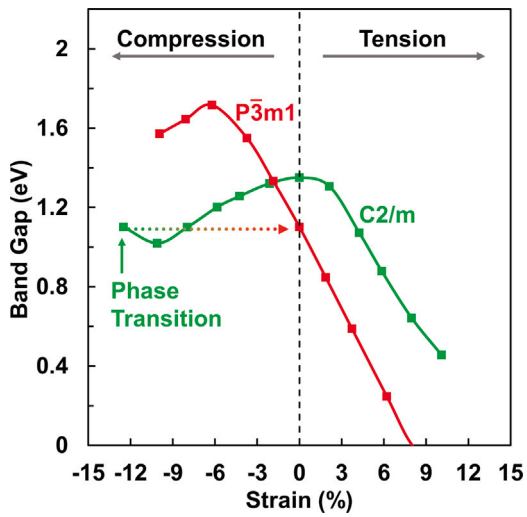

Fig. 8. The variation of electronic band gap (E_g^{PBE}) with respect to uniaxial strain in the armchair direction for C2/m- and P$\bar{3}$m1-GeN monolayer.

bonds in P$\bar{3}$m1-GeN. While the phase transition significantly improves the mechanical properties, the effect on the electronic structure is not drastic. The band gap of P$\bar{3}$m1-GeN is narrower than that of C2/m-GeN but still remains in the visible spectrum. Even the indirect band gap feature is remained, band convergence is noticed for the highest valence of P$\bar{3}$m1-GeN, which might lead to enhanced thermoelectric performance. Our work demonstrates the possibility of realizing the more superior P$\bar{3}$m1 phase of the GeN monolayer by applying strain on a C2/m precursor. This phase can be used in the field of flexible electronic and optoelectronics, involving photocatalytic, photodetector, field effect transistor, and ion-battery applications. The suggested technique could in principle be applicable to the other group IV–V monolayers under properly designed conditions, which broadens the versatility of these materials.

CRediT authorship contribution statement

M. Abboud: Conceptualization, Methodology, Validation, Investigation, Visualization, Writing – original draft, Writing – review & editing. **D.H. Ozbey:** Methodology, Validation, Investigation, Visualization, Writing – review & editing. **E. Durgun:** Conceptualization, Writing – review & editing, Project administration, Supervision, Funding acquisition.

Declaration of competing interest

The authors declare that they have no known competing financial interests or personal relationships that could have appeared to influence the work reported in this paper.

Acknowledgments

This work is supported by the Scientific and Technological Research Council of Turkey (TUBITAK) under Project No. 117F383. The calculations were performed at TUBITAK ULAKBIM, High Performance and Grid Computing Center (TR-Grid e-Infrastructure), and the National Center for High-Performance Computing of Turkey (UHeM) under grant no. 5007092019.

Appendix A. Supplementary data

Supplementary material related to this article can be found online at https://doi.org/10.1016/j.apsusc.2021.150793.

References

[1] C. Barreteau, B. Michon, C. Besnard, E. Giannini, High-pressure melt growth and transport properties of SiP, SiAs, GeP, and GeAs 2D layered semiconductors, J. Cryst. Growth 443 (2016) 75–80.
[2] A.-Q. Cheng, Z. He, J. Zhao, H. Zeng, R.-S. Chen, Monolayered silicon and germanium monopnictide semiconductors: excellent stability, high absorbance, and strain engineering of electronic properties, ACS Appl. Mater. Interfaces 10 (6) (2018) 5133–5139.
[3] S. Zhang, S. Guo, Y. Huang, Z. Zhu, B. Cai, M. Xie, W. Zhou, H. Zeng, Two-dimensional SiP: an unexplored direct band-gap semiconductor, 2D Mater. 4 (1) (2016) 015030.
[4] D. Akinwande, C. Huyghebaert, C.-H. Wang, M.I. Serna, S. Goossens, L.-J. Li, H.-S.P. Wong, F.H. Koppens, Graphene and two-dimensional materials for silicon technology, Nature 573 (7775) (2019) 507–518.
[5] F. Koppens, T. Mueller, P. Avouris, A. Ferrari, M. Vitiello, M. Polini, Photodetectors based on graphene, other two-dimensional materials and hybrid systems, Nat. Nanotechnol. 9 (10) (2014) 780–793.
[6] M. Xu, T. Liang, M. Shi, H. Chen, Graphene-like two-dimensional materials, Chem. Rev. 113 (5) (2013) 3766–3798.
[7] F. Xia, H. Wang, D. Xiao, M. Dubey, A. Ramasubramaniam, Two-dimensional material nanophotonics, Nat. Photonics 8 (12) (2014) 899–907.
[8] C. Li, S. Wang, C. Li, T. Yu, N. Jia, J. Qiao, M. Zhu, D. Liu, X. Tao, Highly sensitive detection of polarized light using a new group IV–V 2D orthorhombic SiP, J. Mater. Chem. C 6 (27) (2018) 7219–7225.
[9] L. Li, W. Wang, P. Gong, X. Zhu, B. Deng, X. Shi, G. Gao, H. Li, T. Zhai, 2D GeP: An unexploited low-symmetry semiconductor with strong in-plane anisotropy, Adv. Mater. 30 (14) (2018) 1706771.
[10] D. Kim, K. Park, F. Shojaei, T.T. Debela, I.S. Kwon, I.H. Kwak, J. Seo, J.P. Ahn, J. Park, H.S. Kang, Thickness-dependent bandgap and electrical properties of GeP nanosheets, J. Mater. Chem. A 7 (27) (2019) 16526–16532.
[11] S. Yang, Y. Yang, M. Wu, C. Hu, W. Shen, Y. Gong, L. Huang, C. Jiang, Y. Zhang, P.M. Ajayan, Highly in-plane optical and electrical anisotropy of 2D germanium arsenide, Adv. Funct. Mater. 28 (16) (2018) 1707379.
[12] H. Sar, J. Gao, X. Yang, In-plane anisotropic third-harmonic generation from germanium arsenide thin flakes, Sci. Rep. 10 (1) (2020) 1–10.
[13] K. Lee, S. Kamali, T. Ericsson, M. Bellard, K. Kovnir, GeAs: Highly anisotropic van der Waals thermoelectric material, Chem. Mater. 28 (8) (2016) 2776–2785.
[14] C.S. Jung, D. Kim, S. Cha, Y. Myung, F. Shojaei, H.G. Abbas, J.A. Lee, E.H. Cha, J. Park, H.S. Kang, Two-dimensional GeAs with a visible range band gap, J. Mater. Chem. A 6 (19) (2018) 9089–9098.
[15] H. Shen, Y. Huang, Y. Chang, R. Hao, Z. Ma, K. Wu, P. Du, B. Guo, Y. Lyu, P. Wang, et al., Narrowing working voltage window to improve layered GeP anode cycling performance for lithium-ion batteries, ACS Appl. Mater. Interfaces 12 (15) (2020) 17466–17473.

[16] K.-H. Nam, K.-J. Jeon, C.-M. Park, Layered germanium phosphide-based anodes for high-performance lithium-and sodium-ion batteries, Energy Storage Mater. 17 (2019) 78–87.

[17] A. Grillo, A. Di Bartolomeo, F. Urban, M. Passacantando, J.M. Caridad, J. Sun, L. Camilli, Observation of 2D conduction in ultrathin germanium arsenide field-effect transistors, ACS Appl. Mater. Interfaces 12 (11) (2020) 12998–13004.

[18] A. Di Bartolomeo, A. Grillo, F. Giubileo, L. Camilli, J. Sun, D. Capista, M. Passacantando, Field emission from two-dimensional GeAs, J. Phys. D: Appl. Phys. 54 (10) (2020) 105302.

[19] J. Guo, Y. Liu, Y. Ma, E. Zhu, S. Lee, Z. Lu, Z. Zhao, C. Xu, S.-J. Lee, H. Wu, et al., Few-layer GeAs field-effect transistors and infrared photodetectors, Adv. Mater. 30 (21) (2018) 1705934.

[20] R. Meng, X. Sun, D. Yang, J. Bao, X. Chen, Two dimensional XAs (X= Si, Ge, Sn) monolayers as promising photocatalysts for water splitting hydrogen production with high carrier mobility, Appl. Mater. Today 13 (2018) 276–284.

[21] L. Zhou, Y. Guo, J. Zhao, GeAs and SiAs monolayers: Novel 2D semiconductors with suitable band structures, Phys. E 95 (2018) 149–153.

[22] N. Jiao, P. Zhou, C. He, J. He, X. Liu, L. Sun, Low-energy GeP monolayers with natural type-II homojunctions for sunlight-driven water splitting, Phys. Status Solidi RRL 13 (12) (2019) 1900470.

[23] B. Mortazavi, M. Shahrokhi, G. Cuniberti, X. Zhuang, Two-dimensional SiP, SiAs, GeP and GeAs as promising candidates for photocatalytic applications, Coatings 9 (8) (2019) 522.

[24] X. Gao, Y. Shen, Y. Ma, S. Wu, Z. Zhou, Theoretical insights into two-dimensional IV–V compounds: Photocatalysts for the overall water splitting and nanoelectronic applications, Inorg. Chem. 58 (18) (2019) 12053–12068.

[25] M. Ashton, S.B. Sinnott, R.G. Hennig, Computational discovery and characterization of polymorphic two-dimensional IV–V materials, Appl. Phys. Lett. 109 (19) (2016) 192103.

[26] M.-s. Miao, J. Botana, E. Zurek, T. Hu, J. Liu, W. Yang, Electron counting and a large family of two-dimensional semiconductors, Chem. Mater. 28 (7) (2016) 1994–1999.

[27] K. Zhang, N. Li, High stability and visible-light photocatalysis in novel two-dimensional monolayer silicon and germanium mononitride semiconductors: first-principles study, RSC Adv. 10 (24) (2020) 14225–14234.

[28] Z. Ma, J. Zhuang, X. Zhang, Z. Zhou, SiP monolayers: New 2D structures of group IV–V compounds for visible-light photohydrolytic catalysts, Front. Phys. 13 (3) (2018) 138104.

[29] S.K. Matta, C. Zhang, Y. Jiao, A. O'Mullane, A. Du, Computational exploration of two-dimensional silicon diarsenide and germanium arsenide for photovoltaic applications, Beilstein J. Nanotechnol. 9 (1) (2018) 1247–1253.

[30] A. Bafekry, F. Shojai, D.M. Hoat, M. Shahrokhi, M. Ghergherehchi, C. Nguyen, The mechanical, electronic, optical and thermoelectric properties of two-dimensional honeycomb-like of XSb (X= Si, Ge, Sn) monolayers: a first-principles calculations, RSC Adv. 10 (51) (2020) 30398–30405.

[31] J.-H. Lin, H. Zhang, X.-L. Cheng, Y. Miyamoto, Single-layer group IV-V and group V-IV-III-VI semiconductors: Structural stability, electronic structures, optical properties, and photocatalysis, Phys. Rev. B 96 (3) (2017) 035438.

[32] P. Wu, M. Huang, Stability, bonding, and electronic properties of silicon and germanium arsenides, Phys. Status Solidi b 253 (5) (2016) 862–867.

[33] M.H. Dalsaniya, T.K. Gajaria, N.N. Som, P.K. Jha, Electron density modulation of a metallic GeSb monolayer by pnictogen doping for excellent hydrogen evolution, Physiol. Chem. Phys. 22 (35) (2020) 19823–19836.

[34] F. Shojaei, H.S. Kang, Electronic structures and li-diffusion properties of group IV–V layered materials: hexagonal germanium phosphide and germanium arsenide, J. Phys. Chem. C 120 (41) (2016) 23842–23850.

[35] J. Zhang, G. Yang, J. Tian, Z. Wang, Y. Tang, D. Ma, Effect of atom adsorption on the electronic, magnetic, and optical properties of the GeP monolayer: A first-principle study, Appl. Surf. Sci. 475 (2019) 863–872.

[36] L.-B. Shi, S. Cao, M. Yang, Strain behavior and carrier mobility for novel two-dimensional semiconductor of GeP: First principles calculations, Phys. E 107 (2019) 124–130.

[37] C. Xu, M. Zhu, J. Zhang, W. Wang, Y. Yan, New two-dimensional allotrope of single layer IV-V semiconductor XBi (X= Si, Ge, Sn), Comput. Mater. Sci. 150 (2018) 314–320.

[38] B. Huang, H.L. Zhuang, M. Yoon, B.G. Sumpter, S.-H. Wei, Highly stable two-dimensional silicon phosphides: Different stoichiometries and exotic electronic properties, Phys. Rev. B 91 (12) (2015) 121401.

[39] B. Mortazavi, T. Rabczuk, Anisotropic mechanical properties and strain tuneable band-gap in single-layer SiP, SiAs, GeP and GeAs, Phys. E 103 (2018) 273–278.

[40] B. Özdamar, G. Özbal, M.N. Çınar, K. Sevim, G. Kurt, B. Kaya, H. Sevinçli, Structural, vibrational, and electronic properties of single-layer hexagonal crystals of group IV and V elements, Phys. Rev. B 98 (4) (2018) 045431.

[41] R.N. Somaiya, Y.A. Sonvane, S.K. Gupta, Exploration of the strain and thermoelectric properties of hexagonal SiX (X= N, P, As, Sb, and Bi) monolayers, Physiol. Chem. Phys. 22 (7) (2020) 3990–3998.

[42] Q.-Y. Chen, C. Cao, Y. He, Optical anisotropy and strain tunable optical, electronic and structural properties in monolayer GeP: A computational study, Phys. E 113 (2019) 172–180.

[43] S. Bai, C.-Y. Niu, W. Yu, Z. Zhu, X. Cai, Y. Jia, Strain tunable bandgap and high carrier mobility in SiAs and SiAs 2 monolayers from first-principles studies, Nanoscale Res. Lett. 13 (1) (2018) 404.

[44] S. Kansara, P.D. Bhuyan, Y. Sonvane, S.K. Gupta, Two-dimensional silicon phosphide: low effective mass and direct band gap for future devices applications, J. Mater. Sci. 54 (18) (2019) 11878–11888.

[45] C. Si, Z. Sun, F. Liu, Strain engineering of graphene: a review, Nanoscale 8 (6) (2016) 3207–3217.

[46] M.A. Bissett, M. Tsuji, H. Ago, Strain engineering the properties of graphene and other two-dimensional crystals, Physiol. Chem. Phys. 16 (23) (2014) 11124–11138.

[47] Y. Sun, K. Liu, Strain engineering in functional 2-dimensional materials, J. Appl. Phys. 125 (8) (2019) 082402.

[48] Z. Dai, L. Liu, Z. Zhang, Strain engineering of 2D materials: issues and opportunities at the interface, Adv. Mater. 31 (45) (2019) 1805417.

[49] R. Roldán, A. Castellanos-Gomez, E. Cappelluti, F. Guinea, Strain engineering in semiconducting two-dimensional crystals, J. Phys.: Condens. Matter. 27 (31) (2015) 313201.

[50] H. Nagai, T. Niimi, Preparation and properties of amorphous germanium nitride films, J. Electrochem. Soc. 115 (6) (1968) 671.

[51] G. Bagratishvili, R. Dzhanelidze, N. Kurdiani, O. Saksaganskii, MIS structure GaAs–Ge3N4–Al, Phys. Status Solidi A 36 (1) (1976) 73–79.

[52] I. Chambouleyron, A. Zanatta, Nitrogen in germanium, J. Appl. Phys. 84 (1) (1998) 1–30.

[53] G. Kresse, J. Furthmüller, Efficient iterative schemes for *ab initio* total-energy calculations using a plane-wave basis set, Phys. Rev. B 54 (16) (1996) 11169.

[54] G. Kresse, D. Joubert, From ultrasoft pseudopotentials to the projector augmented-wave method, Phys. Rev. B 59 (3) (1999) 1758.

[55] G. Kresse, J. Hafner, Ab initio molecular-dynamics simulation of the liquid-metal–amorphous-semiconductor transition in germanium, Phys. Rev. B 49 (20) (1994) 14251.

[56] J. Heyd, G.E. Scuseria, M. Ernzerhof, Hybrid functionals based on a screened Coulomb potential, J. Chem. Phys. 118 (18) (2003) 8207–8215.

[57] A.V. Krukau, O.A. Vydrov, A.F. Izmaylov, G.E. Scuseria, Influence of the exchange screening parameter on the performance of screened hybrid functionals, J. Chem. Phys. 125 (22) (2006) 224106.

[58] H.J. Monkhorst, J.D. Pack, Special points for Brillouin-zone integrations, Phys. Rev. B 13 (12) (1976) 5188.

[59] H.-H. Lee, Finite Element Simulations with ANSYS Workbench 2020, SDC Publications, Mission, KS, USA, 2020.

[60] See Supplemental Material for additional details on stress-strain curves and mechanical response of three GeN phases, strain dependent electronic band structures of GeN monolayers, and the variation of total energy with strain for GeP and GeAs monolayers.

[61] O.C. Zienkiewicz, P. Morice, The Finite Element Method in Engineering Science, vol. 1977, McGraw-Hill London, 1971.

[62] P. Lengvarskỳ, J. Bocko, Prediction of Youngs modulus of graphene sheets by the finite element method, Am. J. Mech. Eng. 3 (6) (2015) 225–229.

[63] L. Chu, J. Shi, S. Ben, Buckling analysis of vacancy-defected graphene sheets by the stochastic finite element method, Materials 11 (9) (2018) 1545.

[64] P. Politzer, S. Ranganathan, Bond-order-bond-energy correlations, Chem. Phys. Lett. 124 (6) (1986) 527–530.

[65] R.L. DeKock, H.B. Gray, Chemical Structure and Bonding, University Science Books, 1989.

[66] T.A. Manz, Introducing DDEC6 atomic population analysis: part 3. Comprehensive method to compute bond orders, RSC Adv. 7 (72) (2017) 45552–45581.

[67] A. Savin, R. Nesper, S. Wengert, T.F. Fässler, ELF: The electron localization function, Angew. Chem., Int. Ed. Engl. 36 (17) (1997) 1808–1832.

[68] S. Noury, X. Krokidis, F. Fuster, B. Silvi, Computational tools for the electron localization function topological analysis, Comput. Chem. 23 (6) (1999) 597–604.

[69] L. Pauling, The Nature of the Chemical Bond, vol. 260, Cornell University Press, Ithaca, NY, USA, 1960.

[70] E. Cadelano, P.L. Palla, S. Giordano, L. Colombo, Elastic properties of hydrogenated graphene, Phys. Rev. B 82 (23) (2010) 235414.

[71] G.N. Greaves, A. Greer, R.S. Lakes, T. Rouxel, Poisson's ratio and modern materials, Nature Mater. 10 (11) (2011) 823–837.

[72] R.M. Christensen, The Theory of Materials Failure, Oxford University Press, Oxford, UK, 2013.

[73] Y. Pei, X. Shi, A. LaLonde, H. Wang, L. Chen, G.J. Snyder, Convergence of electronic bands for high performance bulk thermoelectrics, Nature 473 (7345) (2011) 66.